



Optimization of thermoelectric generator module spacing and spreader thickness used in a waste heat recovery system



Jiin-Yuh Jang*, Ying-Chi Tsai

Department of Mechanical Engineering, National Cheng-Kung University, 1 University Road, Tainan 70101, Taiwan

HIGHLIGHTS

- We provided a 3D numerical model of a TEG module used in a waste heat recovery system.
- The effects of temperature difference and waste gas heat transfer coefficients were investigated.
- The power density for a TEG module is the objective function to be maximized.
- The numerical data are in good agreement (within 8%) with the experimental data.
- The optimum TEG module spacing and spreader thickness are strongly dependent on the waste gas heat transfer coefficient.

ARTICLE INFO

Article history:

Received 22 March 2012
Accepted 15 October 2012
Available online 22 October 2012

Keywords:

Thermoelectric generator module
Spreader
Waste heat recovery
Optimization

ABSTRACT

When thermoelectric generator (TEG) modules are attached to a rectangular chimney plate for venting hot flue gases, the power generated per unit surface area (power density) is strongly dependent on the TEG module spacing. The thermoelectric module consists of a hot plate, a spreader, a thermoelectric generator and a cold plate based on water cooling. In this study, the optimization of TEG module spacing and its spreader thickness as used in a waste heat recovery system is investigated and solved numerically using the finite difference method along with a simplified conjugate-gradient method. The power density for a thermoelectric module is the objective function to be maximized. A search for the optimum module spacing (S) and spreader thickness (H_{sp}), ranging from $40 \text{ mm} < S < 300 \text{ mm}$ and $1 \text{ mm} < H_{sp} < 30 \text{ mm}$, respectively, is performed. The effects of different operating conditions, including the temperature difference between the waste gas and the cooling water ($\Delta T = 200\text{--}800 \text{ K}$), and effective waste gas heat transfer coefficients ($h_h = 20\text{--}80 \text{ W/m}^2 \text{ K}$) are discussed in detail. The predicted numerical data for the power vs. current ($P\text{--}I$) curve are in good agreement (within 8%) with the experimental data.

© 2012 Elsevier Ltd. All rights reserved.

1. Introduction

Thermoelectric generators present potential applications in the conversion of low level thermal energy into electrical power. Especially in the case of waste heat recovery, it is unnecessary to consider the cost of the thermal energy input, and there are additional advantages, such as energy saving and emission reduction, so the low efficiency problem is no longer the most important issue that we have to take into account [1]. In general, a TEG consists of a number of semiconductor pairs that are connected electrically in a series and thermally in parallel, and each pair includes a p-type and an n-type element. Although in theory, a single piece of

semiconductor material could work, a series connection is used to meet the high voltage potential requirements. p-Type and n-type elements are alternated to assure that the carriers transport in the same direction.

Most of the reported performance data of TEGs is analyzed using conventional non-equilibrium thermodynamics [2,3]. With reference to the structure of a TEG, a significant increase in the power output from a module can be achieved by modifying the geometry of the thermoelectric elements [4,5]. In subsequent research, Rowe [6,7] provided efficiency in a couple of solar-powered TEGs and reviewed applications of nuclear-powered TEGs in space. Chen et al. [8] used an irreversible model to study the performance of a TEG with external and internal irreversibility. The optimal range of the parameters for the device-design was determined, and the problems relative to the maximum power output and maximum efficiency were discussed. Xuan et al. [9] employed

* Corresponding author. Tel.: +886 6 2757575x62148; fax: +886 6 2088573.
E-mail address: jangjim@mail.ncku.edu.tw (J.-Y. Jang).

Nomenclature		Greek symbols	
A	TEG module area (mm^2) $A = S \times S$	α	Seebeck coefficient (V/K)
D_h	hydraulic diameter (m)	β	descend direction coefficient
E	electric field (V/m)	ε	flue gas emissivity
h	effective heat transfer coefficient ($\text{W/m}^2 \text{K}$)	η	TEG conversion efficiency (%) $\eta = P_{\max}/Q_h$
H	height (mm)	ϕ	general dependent
I	electric current (A)	ρ	electrical resistivity (Ωm)
\bar{J}	electric current density (A/m^2)	σ	Stefan Boltzmann constant ($\text{W/m}^2 \text{K}^4$)
J_{obj}	objective function	ξ	search directions
k	thermal conductivity (W/m K)	Subscripts	
L	length (mm)	c	cold side
n	pairs of p-type and n-type semiconductor	cer	ceramic substrate
P	power output (W)	$cond$	conductive copper
P_{\max}	maximum power output (W)	$conv$	convection
P_{\max}/A	maximum power density (W/m^2)	f	fluid
Q	heat transfer rate (W)	gas	flue gas
R	residual sum	h	hot side
S	TEG module spacing (mm)	hp	hot plate
T	temperature (K)	opt	optimal design
ΔT	temperature difference between the waste gas and the cooling water (K)	$P-N$	p- and n-type thermoelectric semiconductor
V	electric potential (V)	rad	radiation
v	velocity (m/s)	sp	spreader
V_{oc}	open circuit voltage (V)	TEG	thermoelectric generator
x_i	design variable vector	$water$	cooling water
x, y, z	Cartesian coordinates		

a phenomenological model to study the effects of internal and external interface layers on thermoelectric module performance. Sets of general performance formulas have also been derived. Pramanick and Das [10] performed a study on the structural design of a thermoelectric module. A model for a cascaded TEG was developed, which was based on finite time thermodynamics.

Recently, there has been a growing interest in TEGs using various heat sources in such applications as combustion of waste, geothermal energy, power plants, and other industrial heat-generating processes [11,12]. Khattab and Shenawy [13] studied the possibility of using a solar TEG to drive a small thermoelectric cooler (TEC). Crane and Jackson [14] studied numerical heat exchanger models integrated with models for Bi_2Te_3 thermoelectric modules which were validated against experimental data from previous cross-flow heat exchanger studies as well as experiments using thermoelectric modules between counter-flow hot water and cooling air flow channels. Dai et al. [15] provided a new type of TEG system based on liquid metal which served to harvest and transport waste heat. The experimental results for the TEG system were discussed and a calculated efficiency of 2% in the whole TEG system was obtained. Champier et al. [16] reported a study conducted in order to investigate the feasibility of using a TEG in an improved biomass fired stove. The maximum power reached by each module varied between 1.7 W and 2.3 W, resulting in a temperature difference between the two sides of 160 °C.

Furthermore, in the application of TEGs for waste heat recovery power generation, there have been many conceptual designs for a power conversion system that are potentially capable of being applied in this area. Hsiao et al. [17] constructed a mathematic model to predict the performance of a TEG module attached to a waste heat recovery system. The results showed that the TEG module presented better performance on an exhaust pipe as opposed to a radiator. Thacher et al. [18] investigated the feasibility of waste heat recovery from exhaust in a light truck by connecting

a series of 16 TEG modules, which showed good performance at high speeds. Niu et al. [19] constructed an experimental TEG unit, which was used to examine the influences of the main operating conditions, the hot and cold fluid inlet temperatures, flow rates and the load resistance on the power output and conversion efficiency. Karri et al. [20] studied the power and fuel savings produced by TEGs placed in the exhaust stream of a sports utility vehicle (SUV). The optimized quantum-well (QW) based TEG stack generated about 5.3–5.8 kW, resulting in a fuel savings of about 3%.

According to the literature survey [21], it is recognized that most of the previous theoretical models have been limited to one dimensional problems. However, in these existing models, the $P-N$ element pair is simply treated as a single bulk material so that the difference in thermal behavior between the two semiconductor elements was not possible to evaluate. Only a few studies have been conducted for three-dimensional TEGs. For example, Chen et al. [22] proposed a three-dimensional TEG model and implemented it in a computational fluid dynamics simulation environment (FLUENT) and its user-defined functions (UDFs). Cheng et al. [23] provided a three-dimensional numerical model to predict transient thermal behavior of TECs. It was observed that both the temperatures of the hot and the cold ends increased with the cooling load, and the value of the COP (coefficient of performance) linearly increased with the cooling load. Recently, Sidek et al. [24] provided a numerical study on temperature uniformity of thermal spreader integration with microcombustor for TEG. The results show the effect of thermal conductivity, specific heat capacity and thickness, and the mutual relation between the magnitude of heat source and thermal spreader temperature profile. Jang et al. [25] used a numerical optimization technique in a geometrical optimization for spreaders to obtain efficient power output balancing with reasonable material costs. The results showed the optimum spreader length and thickness with the fixed module spacing for Pareto-optimal configurations.

In the present study, the optimization of TEG module spacing and its spreader thickness is investigated and solved numerically using the finite difference method along with a simplified conjugate-gradient method (SCGM) [26]. To reach optimization goals, the power density for the thermoelectric module is the objective function to be maximized. The effects of different operating conditions, including the temperature difference between the waste gas and the cooling water ($\Delta T = 200\text{--}800\text{ K}$), and effective waste gas heat transfer coefficients ($h_h = 20\text{--}80\text{ W/m}^2\text{ K}$) are investigated and discussed in detail. In addition, experiments are conducted to verify the physical model.

2. Mathematical analysis for the thermoelectric module

The schematic diagram of a waste heat recovery system with thermoelectric modules is shown in Fig. 1. The thermoelectric module consists of a hot plate, a spreader, a TEG and a cold plate based on water cooling. The dimensions of the assembled square TEG unit are $30\text{ mm} \times 30\text{ mm} \times 3.42\text{ mm}$. Its material is Bi_2Te_3 and the detailed geometrical parameters and thermal–electrical

properties of the TEG module are listed in Table 1. A TEG is the major component of the thermoelectric module, in which 31 pairs of p-type and n-type semiconductor legs composing the generator are connected thermally in parallel between the hot waste gas and cold plate and electrically in a series to power the load circuit. Since we use the thermoelectric models on the basis of an equivalent current method, which means there is an equal electric current and an equal cross area of thermoelectric elements, only one pair is considered here. Table 2 shows the equivalent thermal–electrical properties (thermal conductivity k_{P-N} , electrical resistivity ρ_{P-N} and Seebeck coefficient α_{P-N}) when a TEG module with n pairs of p-type and n-type semiconductors is simplified to one pair, where $n = 31$ in the present study.

2.1. Governing equations

Assuming constant thermal and electrical properties of the thermoelectric material, the governing equation of the thermal field (T) and electrical potential (V) for the p-type and n-type element can be expressed as

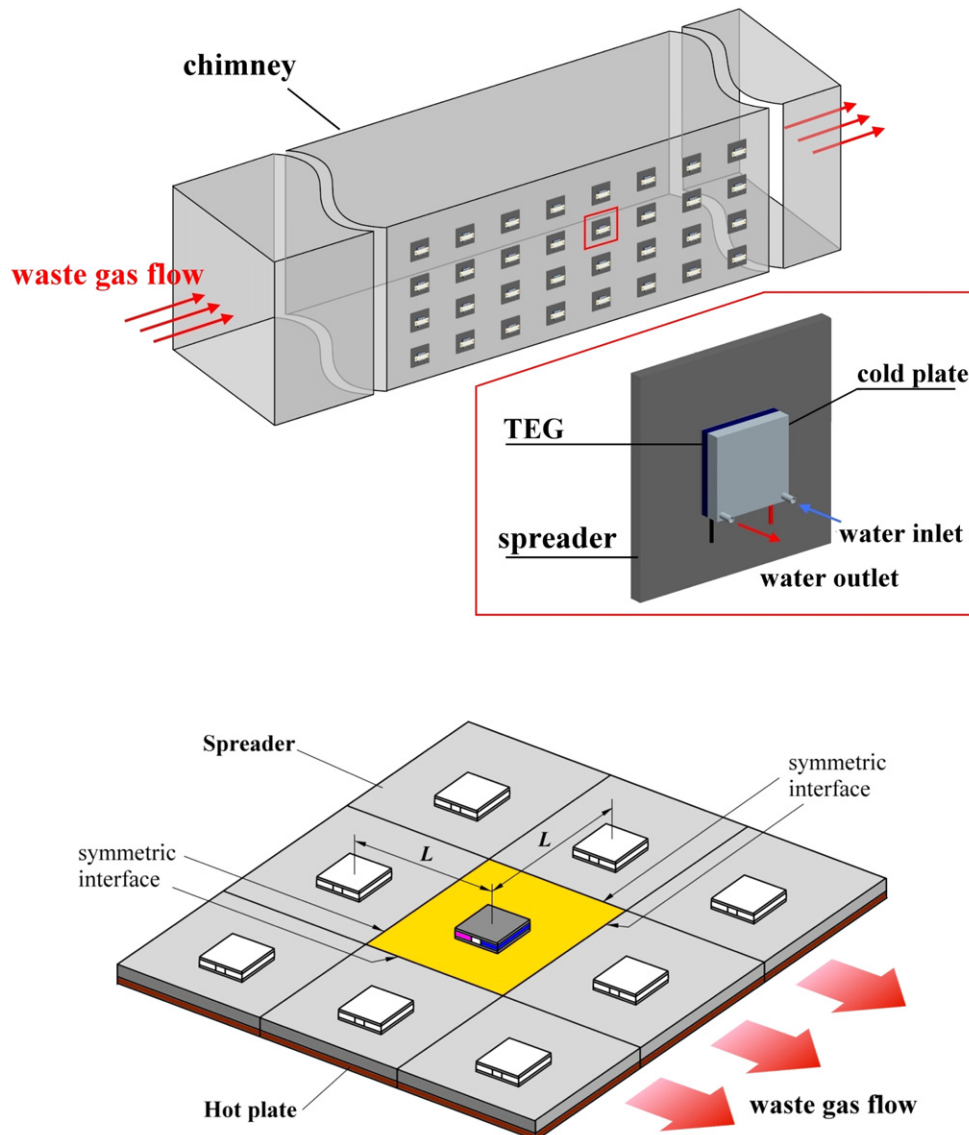


Fig. 1. Schematic diagram of the thermoelectric module with a spreader for waste heat recovery.

Table 1
Geometrical parameters and thermal–electrical properties of the TEG module.

Geometrical and thermal–electrical properties	Symbol	Value
1. Hot plate		
Thickness (mm)	H_{hp}	30
Thermal conductivity (W/m K)	k_{hp}	43 (Steel)
2. Spreader		
Thermal conductivity (W/m K)	k_{sp}	155 (Aluminum)
3. Ceramic substrate		
Thickness (mm)	H_{cer}	0.75
Thermal conductance (W/m K)	k_{cer}	49.2
4. Conductive copper		
Thickness (mm)	H_{cond}	0.12
Thermal conductance (W/m K)	k_{cond}	403
Seebeck coefficient (V/K)	α_{cond}	1.4×10^{-5}
Resistivity (Ω m)	ρ_{cond}	1.44×10^{-8}
5. P–N thermoelectric elements (for one pair)		
Thickness (mm)	H_{p-N}	1.68
Thermal conductance (W/m K)	k_{p-N}	1.6
Seebeck coefficient (V/K)	α_{p-N}	$\pm 2.0 \times 10^{-4}$
Electrical resistivity (Ω m)	ρ_{p-N}	9.0×10^{-6}

$$k_{p-N} \left(\frac{\partial^2 T}{\partial x^2} + \frac{\partial^2 T}{\partial y^2} + \frac{\partial^2 T}{\partial z^2} \right) + \rho_{p-N} \vec{J}^2 = 0 \quad (1)$$

$$\begin{aligned} \vec{E} &= - \left(\frac{\partial V}{\partial x} \vec{i} + \frac{\partial V}{\partial y} \vec{j} + \frac{\partial V}{\partial z} \vec{k} \right) - \alpha_{p-N} \left(\frac{\partial T}{\partial x} \vec{i} + \frac{\partial T}{\partial y} \vec{j} + \frac{\partial T}{\partial z} \vec{k} \right) \\ &= \rho_{p-N} \vec{J} \end{aligned} \quad (2)$$

where k_{p-N} , ρ_{p-N} and α_{p-N} represent the equivalent thermal conductivity, electrical resistivity and Seebeck coefficient of TEG module with 31 pairs of p-type and n-type semiconductors, respectively. The E and J denote the electrical field and current density, respectively.

The energy heat conductions for the solid spreader, ceramic substrate and conductive copper are

$$\frac{\partial^2 T}{\partial x^2} + \frac{\partial^2 T}{\partial y^2} + \frac{\partial^2 T}{\partial z^2} = 0 \quad (3)$$

2.2. Boundary conditions

(1) At the bottom surface of hot plate.

$$-k_{hp} \frac{\partial T}{\partial y} = h_h (T_{gas} - T) \quad (4)$$

Table 2
The equivalent thermal–electrical properties when the TEG module with n pairs of p-type and n-type semiconductors is simplified to one pair.

Thermo-electrical property	p-Type and n-type (for one pair)	When TEG with n pairs is simplified to 1 pair
Thermal conductivity (W/m K)	k_{p-N}	k_{p-N} (Unchanged)
Electrical resistivity (Ω m)	ρ_{p-N}	$n^2 \rho_{p-N}$
Seebeck coefficient of (V/K)	α_{p-N}	$n \alpha_{p-N}$

where h_h is the effective heat transfer coefficient combining the radiation (h_{rad}) and convection (h_{conv}) heat transfer coefficients, which may be estimated as follows [27]:

$$h_{rad} = \sigma \cdot \varepsilon \cdot (T_s + T_{gas}) \cdot (T_s^2 + T_{gas}^2) \quad (5a)$$

$$Nu = 0.023 Re^{0.8} Pr^{1/3} = \frac{h_{conv} \cdot D_h}{k_f} \quad \text{Dittus–Boelter equation} \quad (5b)$$

where σ is the Stefan Boltzmann constant, and ε is the flue gas emissivity. The Reynolds number is $Re = vD_h/\nu$ and Pr is the Prandtl number. D_h and k_f are represent the hydraulic diameter and thermal conductivity of the fluid, respectively. It can be shown that for T_{gas} ranging from 500 to 1100 K and flue gas velocity ranging from 1 to 5 m/s, the effective heat transfer coefficient h_h is ranging from 20 to 80 W/m² K.

(2) At the interface between the hot plate and spreader, there is a continuity of temperature and heat flux.

$$T_{sp} = T_{hp} \quad \text{and} \quad -k_{sp} \frac{\partial T}{\partial y} = -k_{hp} \frac{\partial T}{\partial y} \quad (6)$$

(3) At the interface between spreader and ceramic substrate.

$$T_{cer} = T_{sp} \quad \text{and} \quad -k_{cer} \frac{\partial T}{\partial y} = -k_{sp} \frac{\partial T}{\partial y} \quad (7)$$

(4) At interface between ceramic substrate and conductive copper.

$$T_{cer} = T_{cond} \quad \text{and} \quad -k_{cer} \frac{\partial T}{\partial y} = -k_{cond} \frac{\partial T}{\partial y} \quad (8)$$

(5) At the interface between conductive copper and p-type and n-type thermoelectric elements,

$$\begin{aligned} T_p &= T_{cond} \quad \text{and} \quad -k_p \frac{\partial T}{\partial y} \\ &= -k_{cond} \frac{\partial T}{\partial y} - J(\alpha_p - \alpha_{cond})T \quad (\text{for p-type}) \end{aligned} \quad (9)$$

$$\begin{aligned} T_n &= T_{cond} \quad \text{and} \quad -k_n \frac{\partial T}{\partial y} \\ &= -k_{cond} \frac{\partial T}{\partial y} - J(\alpha_n - \alpha_{cond})T \quad (\text{for n-type}) \end{aligned} \quad (10)$$

The last terms in the right side of eqs. (9) and (10) are the Peltier heat due to the current flow through two different materials with different Seebeck coefficients.

(6) At the top surface of the TEG.

$$-k_{cer} \frac{\partial T}{\partial y} = h_c (T - T_{water}) \quad (11)$$

where h_c and T_{water} represent the heat transfer coefficient and cooling water temperature, respectively. Additionally, the h_c can be estimated from the Dittus–Boelter equation, eq. (5b). For water velocity $v = 0.2$ m/s and $D_h = 10$ mm, the h_c is around 1000 W/m² K.

(7) At the symmetrical planes normal gradients are equal to zero. In addition, all remaining surfaces are set to be adiabatic conditions.

(8) The boundary condition for the voltage is $V = 0$ V at p-type thermoelectric element.

2.2.1. Performance of a TEG

The performance of a thermoelectric generator can be characterized. The power generated from a thermoelectric generator can be calculated as follows:

$$P = I \cdot V \quad (12)$$

The TEG conversion efficiency is given by

$$\eta = \frac{P}{Q_h} \quad (13)$$

where Q_h is the heat transfer rate of the hot side

$$Q_h = -k_{hp} A \frac{\partial T}{\partial y} \quad (14)$$

2.3. Numerical methods

Since there is no analytical solution in this study, the governing equations eqs. (1) and (3) along with the boundary conditions eqs. (4)–(11) are solved numerically using the finite difference method. Fig. 2 shows the physical model and computation grid system for the thermoelectric module with the spreader in Cartesian coordinates. A grid system of 83,722 grid points was adopted typically in the computation domain. Here, the grid pattern is coarsely displayed for the convenience of the reader to visualize the computational regions.

Prior to computation, a thorough verification of the grid-independence of the numerical solution is performed in order to ensure the accuracy and validity of the numerical results. A grid system of 83,722 grid points is typically adopted in the computational domain. In order to validate the independency of the solution on the grid, three different grid systems are investigated, which include about 61,636, 83,722 and 100,954 nodes, respectively, for a thermoelectric module with a spreader. It is found that the relative errors in the local temperature (T) and electric potential (V) between the solutions of 83,722 and 100,954 are less than 3.0%. Computations were performed on an INTEL Core i7-2600 3.40G personal computer, and typical CPU times were about 1500 s for each case.

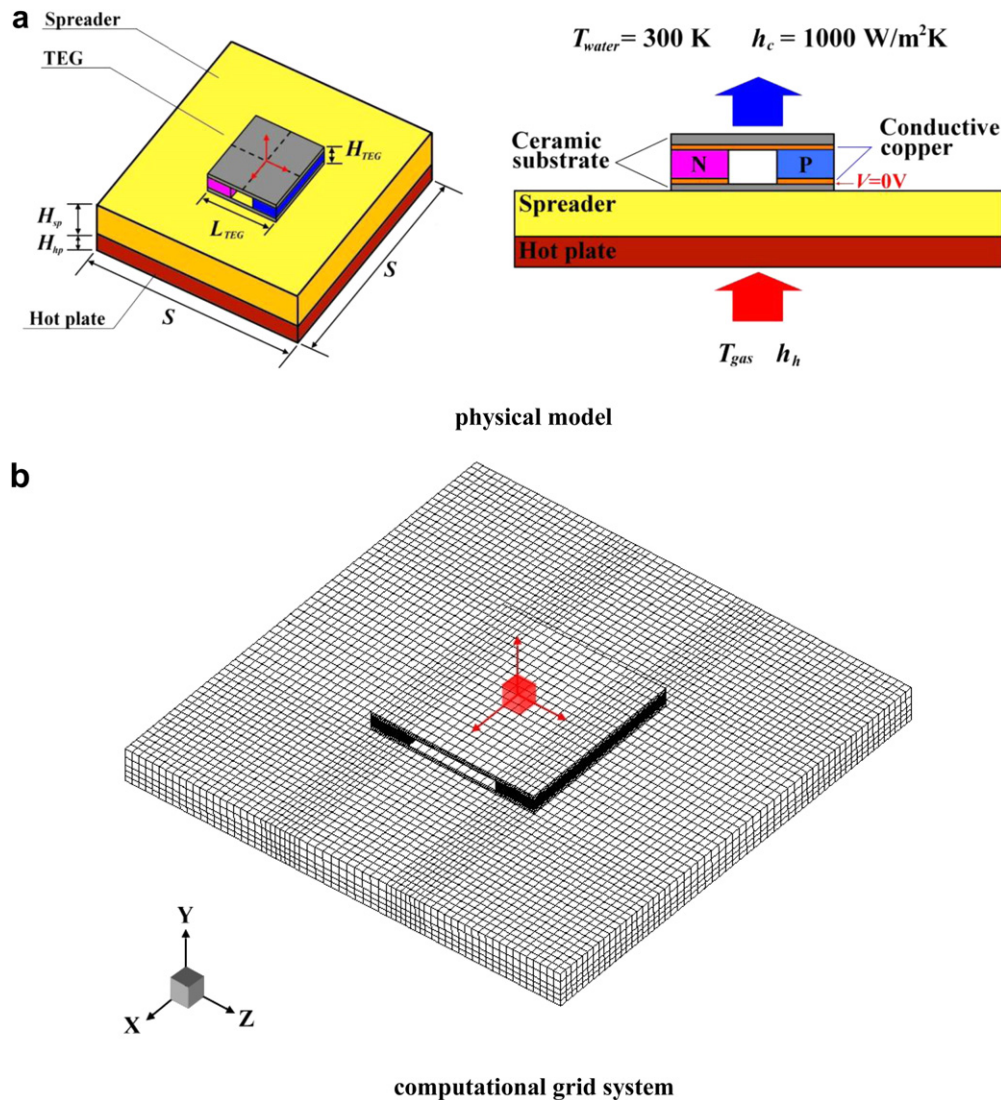


Fig. 2. The physical model and computational grid system.

3. Optimization

In the present study, the simplified conjugate-gradient method (SCGM) [26] has been combined with finite difference method (FDM) code as an optimizer to search the optimum TEG module spacing (S) and corresponding spreader thickness (H_{sp}). The objective functions $J_{obj}(x_1, x_2)$ are defined as the maximum power per unit surface area (i.e. the maximum power density, P_{max}/A).

Above all, the SCGM method evaluates the gradient of the objective function, and then it sets up a new conjugate direction for the updated design variables with the help of a direct numerical sensitivity analysis. The initial guess for the value of each search variable is made, and in the successive steps, the

conjugate-gradient coefficients and the search directions are evaluated to estimate the new search variables. The solutions obtained from the finite difference method are then used to calculate the value of the objective function, which is further transmitted back to the optimizer for the purpose of calculating the consecutive searching directions. The procedure for applying this method is described in the following:

- (1) Generate an initial guess for two design variables (x_1, x_2) – TEG module spacing (S) and its spreader thickness (H_{sp}).
- (2) Adopt the finite difference method to predict the temperature fields (T) and electric potential (V) associated with the latest S and H_{sp} , and then calculate the objective function $J_{obj}(x_1, x_2)$.

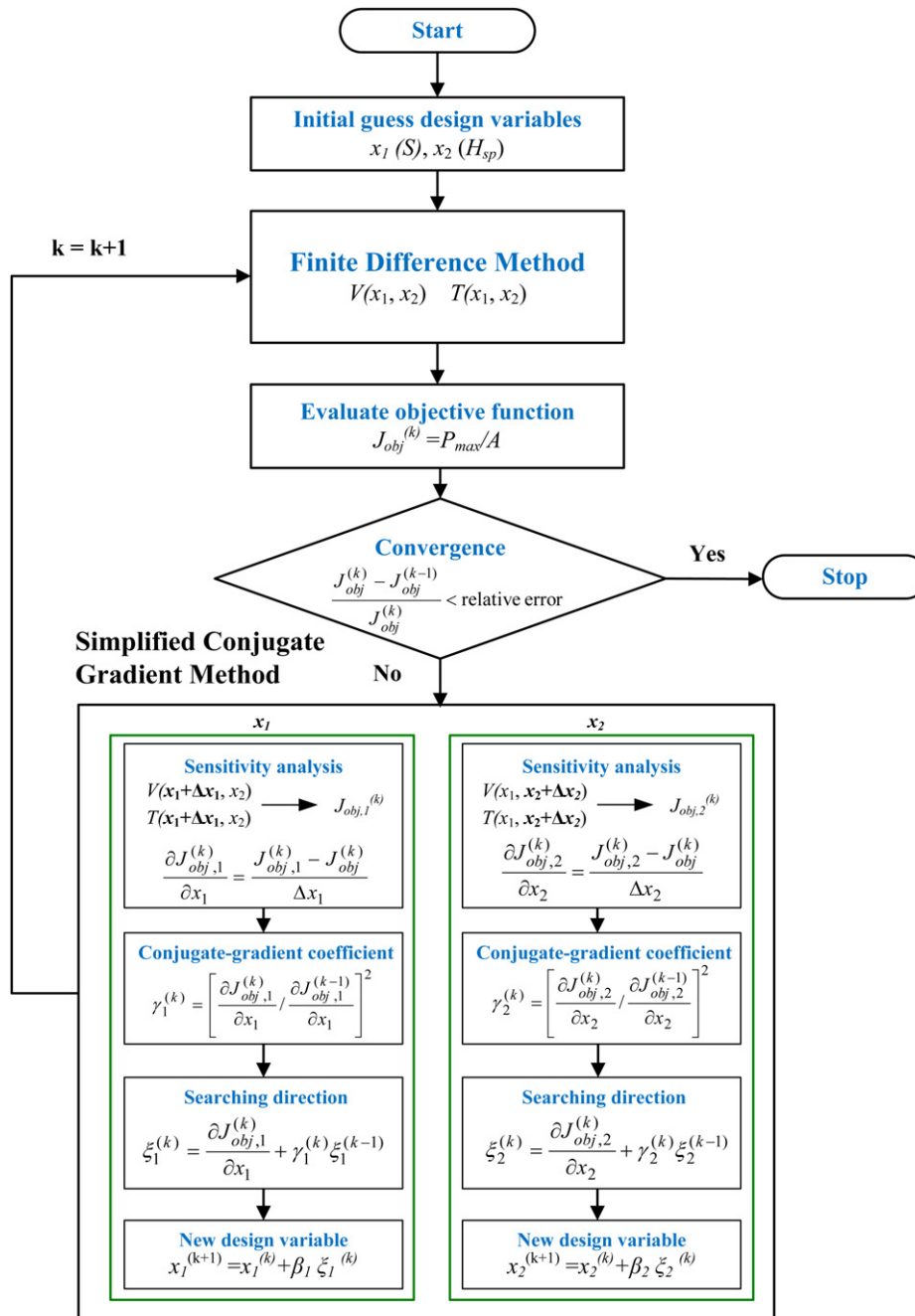


Fig. 3. Flow charts for the optimization method.

- (3) When the value of $J_{obj}(x_1, x_2)$ reaches a maximum, the optimization process is terminated. Otherwise, proceed to step (4).
- (4) Determine the gradient functions, $(\partial J_{obj}/\partial x_1)^{(k)}$ and $(\partial J_{obj}/\partial x_2)^{(k)}$, by applying a small perturbation $(\Delta x_1, \Delta x_2)$ to each value of x_1 and x_2 , and calculate the corresponding change in objective function (ΔJ_{obj}) . Then, the gradient function with respect to each value of the design variables (x_1, x_2) can be calculated by the direct numerical differentiation as

$$\frac{\partial J_{obj}}{\partial x_1} = \frac{\Delta J_{obj}}{\Delta x_1} \quad \text{and} \quad \frac{\partial J_{obj}}{\partial x_2} = \frac{\Delta J_{obj}}{\Delta x_2} \quad (15)$$

- (5) Calculate the conjugate-gradient coefficients, $\gamma_1^{(k)}$ and $\gamma_2^{(k)}$, and the search directions, $\xi_1^{(k+1)}$ and $\xi_2^{(k+1)}$, for each search variable. For the first step with $k = 1$, $\gamma_1^{(1)} = 0$ and $\gamma_2^{(1)} = 0$.

$$\gamma_1^k = \left[\frac{(\partial J_{obj}/\partial x_1)^k}{(\partial J_{obj}/\partial x_1)^{k-1}} \right]^2 \quad \text{and} \quad \gamma_2^k = \left[\frac{(\partial J_{obj}/\partial x_2)^k}{(\partial J_{obj}/\partial x_2)^{k-1}} \right]^2 \quad (16)$$

$$\xi_1^{k+1} = \frac{\partial J_{obj}^k}{\partial x_1} + \gamma_1^k \xi_1^k \quad \text{and} \quad \xi_2^{k+1} = \frac{\partial J_{obj}^k}{\partial x_2} + \gamma_2^k \xi_2^k \quad (17)$$

- (6) Assign values to the coefficients of descent direction (β_1, β_2) for all values of the design variables (x_1, x_2) . Specifically, those values are chosen by a trial-and-error process. In general, the coefficients of descent direction (β_1, β_2) are within a range of 0.01–0.001.
- (7) Update the design variables with

$$x_1^{(k+1)} = x_1^{(k)} + \beta_1 \xi_1^{(k)} \quad \text{and} \quad x_2^{(k+1)} = x_2^{(k)} + \beta_2 \xi_2^{(k)} \quad (18)$$

A flowchart of the SCGM optimization process is plotted in Fig. 3.

4. Experiment setup and uncertainty analysis

As illustrated in Fig. 4, the wind tunnel system consists of a blower, 12 annular heaters (35 kW), a settling chamber, the TEG

module and an exhaust pipe. The air flow was driven by a 3.7 kW centrifugal fan with an inverter to provide various inlet velocities. During the isothermal test, it was determined that the variations in the temperature in different locations were within $\pm 0.2^\circ\text{C}$ and that a free stream turbulence intensity of less than 2% was achieved. The air temperatures at the inlet and the exit zones across the test section were measured by two pre-calibrated RTDs (pt-100 Ω). Their accuracy was within $\pm 0.05^\circ\text{C}$. The desired air velocity through the test section was set by means of adjusting an inverter. The air velocity was measured by a hot wire with $\pm 2.0\%$ accuracy. To reduce heat loss, all wind tunnel system was surrounded by insulators.

The TEG module was cooled by water, and its temperature was controlled at 27°C by a thermostat reservoir. The water volumetric flow rate was measured by a magnetic volume flow meter with 0.002 L/s resolution. The heat transfer coefficients in the water channel (h_c) and wind tunnel (h_h) could be estimated by using the Dittus–Boelter equation. A high power electrical resistor array was connected in series to the system which was used to capture the matching load for the optimized power output. The ammeter and the voltmeter were connected to measure the current in the circuit and voltage cross the external load resistor respectively. A digital multi-meter (Fluke 170) was used to measure the voltage with an accuracy of 0.15% and the current with an accuracy of 1.0%. All the data signals were collected and converted using a data acquisition system (a hybrid recorder).

As estimating the uncertainty in measured and calculated quantities, the bias and precision errors were both considered. These elemental errors are combined to obtain an overall uncertainty in a measured quantity using the root-sum-squares (RSS) method. Uncertainties in the reported experimental values of effective heat transfer coefficient (h) and power output (P) as estimated by the method suggested by Moffat [28]. The uncertainties are tabulated in Table 3. To minimize the precision uncertainty of a measurement, the experiment was measured ten times in the same way and in the same circumstance and taking the average.

5. Results and discussion

Fig. 5(a) and (b) illustrates the temperature and electric potential distributions of the thermoelectric module with and without the spreader, respectively, for a TEG module spacing $S = 200$ mm,

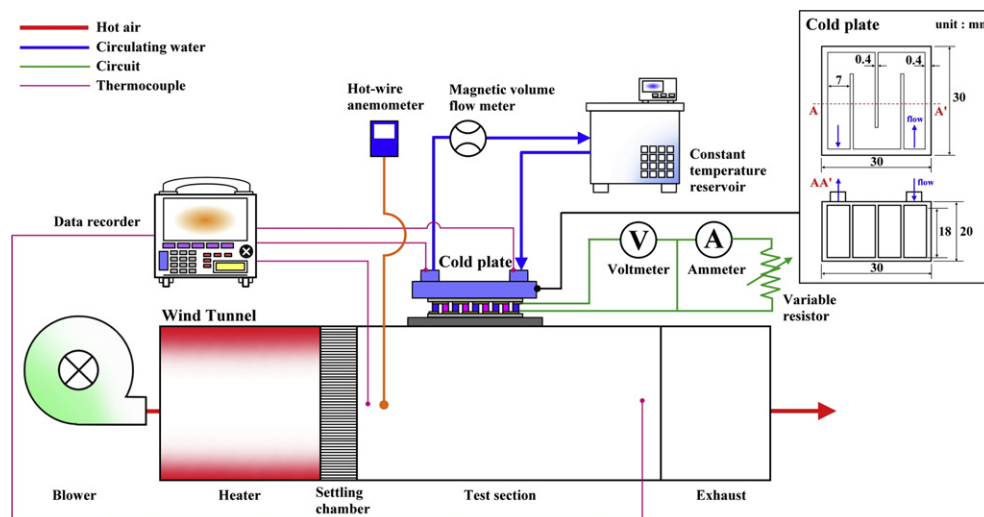


Fig. 4. Schematic diagram of the experimental setup.

Table 3
Summary of estimated uncertainties.

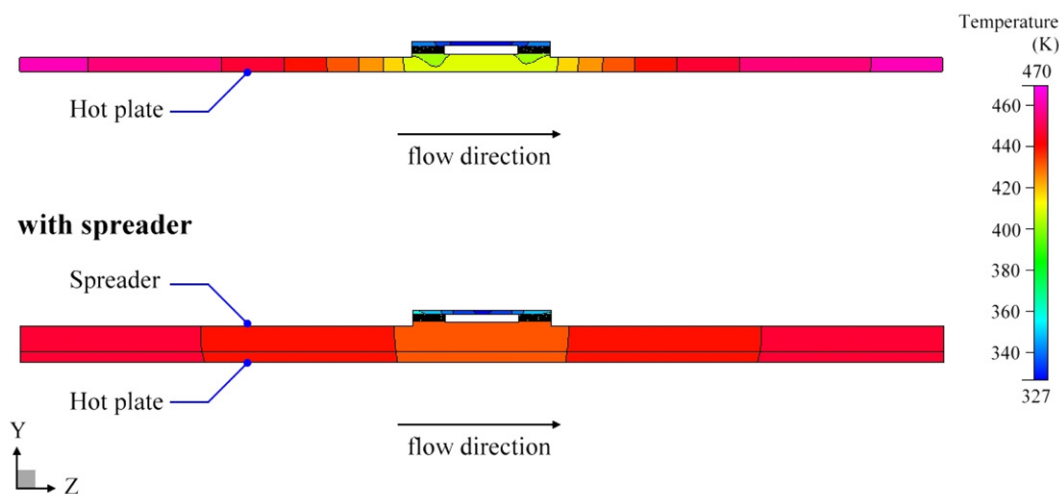
Primary measurements		Derived quantities		
Parameter	Uncertainties	Parameter	Uncertainties	Uncertainties
			$Re_{gas} = 1000$	$Re_{gas} = 5000$
$V_{fr, gas}$	0.3–1%	Re_{gas}	$\pm 1.2\%$	$\pm 0.41\%$
\dot{m}_{water}	0.5%	Q_{gas}	$\pm 3.5\%$	$\pm 1.6\%$
I	0.2%	h_h	$\pm 5.6\%$	$\pm 2.2\%$
V	0.1%	P	$\pm 0.22\%$	$\pm 0.22\%$
T_{gas}	0.1 °C			
T_{water}	0.05 °C			

and its spreader thickness $H_{sp} = 5$ mm, where the hot and cold surfaces were assumed to be exposed to heat transfer with convective heat transfer coefficient $h_h = 20$ W/m² K for the hot side and $h_c = 1000$ W/m² K for the cold side and with a temperature

difference ($\Delta T = 200$ K). It is seen from Fig. 5(a) that a proper size of heat spreader can indeed decrease the total thermal resistance due to a larger heat conduction cross section area from the hot gas side to the cold water side. Thus, the temperature difference between the top and bottom surfaces of the TEG with a spreader is 103 K, which is larger than that without a spreader (87 K). This results in an open circuit voltage $V_{oc} = 1.133$ V (21% increase) for a TEG module with a spreader compared to $V_{oc} = 0.935$ V for the one without a spreader, as seen in Fig. 5(b).

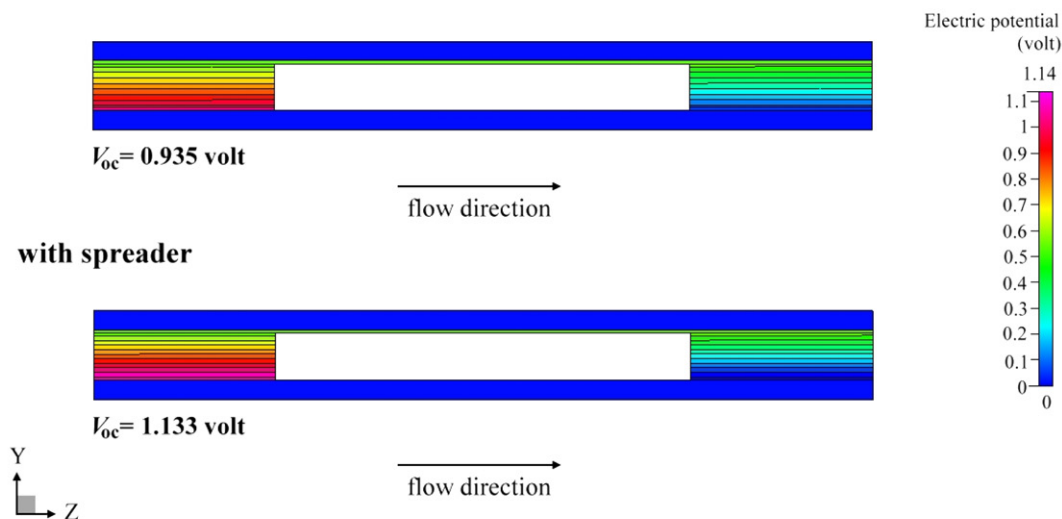
Fig. 6(a) and (b) shows the voltage–current ($V-I$) and power–current ($P-I$) curves, respectively, for three different values of temperature difference between the waste gas and the cooling water ($\Delta T = 100$ K, 150 K and 200 K) with $S = 200$ mm, $H_{sp} = 5$ mm and $h_h = 20$ W/m² K. The dashed lines denote the results without a spreader. In addition, the experimental results are denoted by circle symbols. It can be seen that the predicted numerical data for

a without spreader



the temperature distribution

b without spreader



the electric potential distribution of TEG

Fig. 5. The temperature and electric potential distributions for the thermoelectric module with and without the spreader, respectively, for $S = 200$ mm, $H_{sp} = 5$ mm, $h_h = 20$ W/m² K and $\Delta T = 200$ K.

the $V-I$ and $P-I$ curves are in good agreement (within 8%) with the experimental data. It can be found that the maximum power, P_{max} , occurs when the external load resistance is equal to the effective internal resistance of the TEG. A close look at Fig. 6(b) indicates that the P_{max} with a spreader can be significantly increased up to 50% compared to those without a spreader.

Fig. 7(a)–(c) presents the variations of P_{max} , η and P_{max}/A with the TEG module spacing module spacing (S), respectively, for four different values of waste gas heat transfer coefficients ($h_h = 20, 40,$

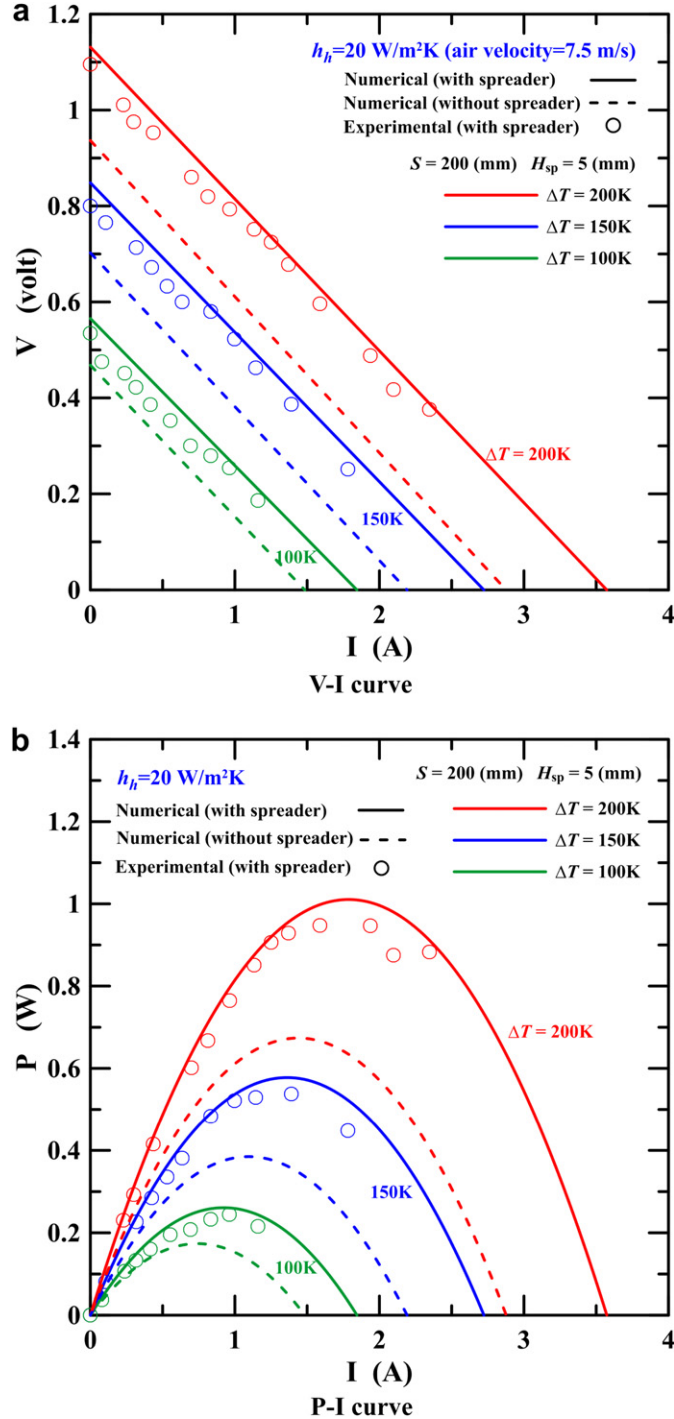


Fig. 6. $V-I$ and $P-I$ curves for different values of temperature differences between the waste gas and the cooling water with $S = 200 \text{ mm}$, $H_{sp} = 5 \text{ mm}$ and $h_h = 20 \text{ W/m}^2\text{K}$.

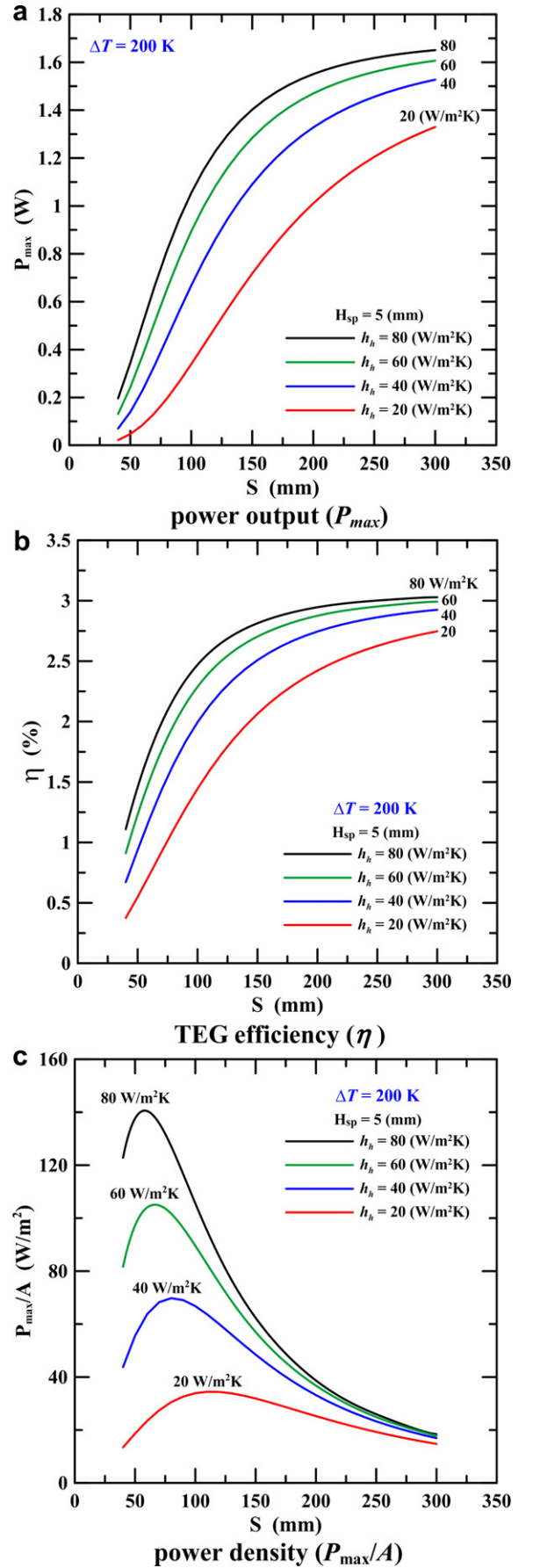


Fig. 7. The P_{max} , η and P_{max}/A vs. TEG module spacing (S) for different values of waste gas heat transfer coefficients with $H_{sp} = 5 \text{ mm}$ and $\Delta T = 200 \text{ K}$.

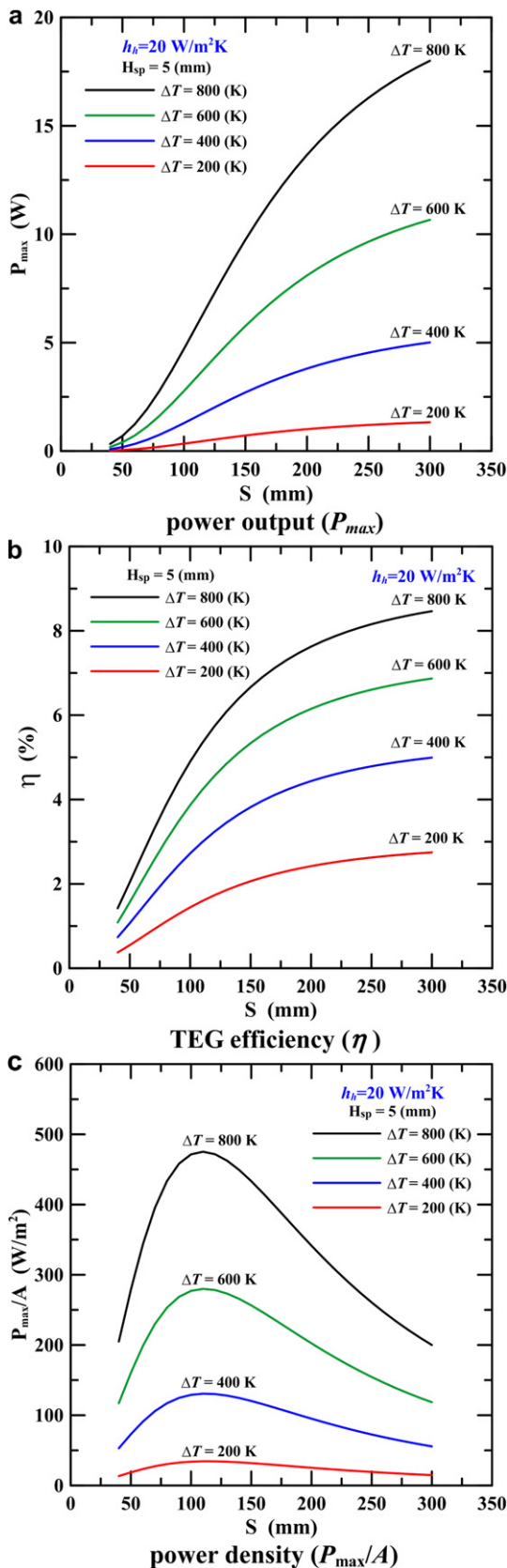


Fig. 8. The P_{max} , η and P_{max}/A vs. TEG module spacing (S) for different values of temperature differences between the waste gas and the cooling water with $H_{sp} = 5 \text{ mm}$ and $h_h = 20 \text{ W/m}^2\text{K}$.

60 and 80 $\text{W/m}^2\text{K}$) with a spreader thickness $H_{sp} = 5 \text{ mm}$ and $\Delta T = 200 \text{ K}$. As expected, both the power output and TEG efficiency (η) are increased as either the module spacing (S) or the waste gas heat transfer coefficient (h_h) is increased (this corresponds to a larger heat transfer area $A = S^2$ or a higher waste gas velocity). However, there is an asymptotic nature of the P_{max} – S curves when S is greater than around 150 mm. Thus, there is optimum module spacing S for the maximum power density (P_{max}/A), as seen from Fig. 7(c). As an example, for $H_{sp} = 5 \text{ mm}$ and $\Delta T = 200 \text{ K}$, the optimal module spacing S is about 110 mm for $h_h = 20 \text{ W/m}^2\text{K}$, while the optimum S is about 60 mm for $h_h = 80 \text{ W/m}^2\text{K}$.

Fig. 8(a)–(c) demonstrates the variations in P_{max} , η and P_{max}/A with the TEG module spacing (S) for four temperature differences

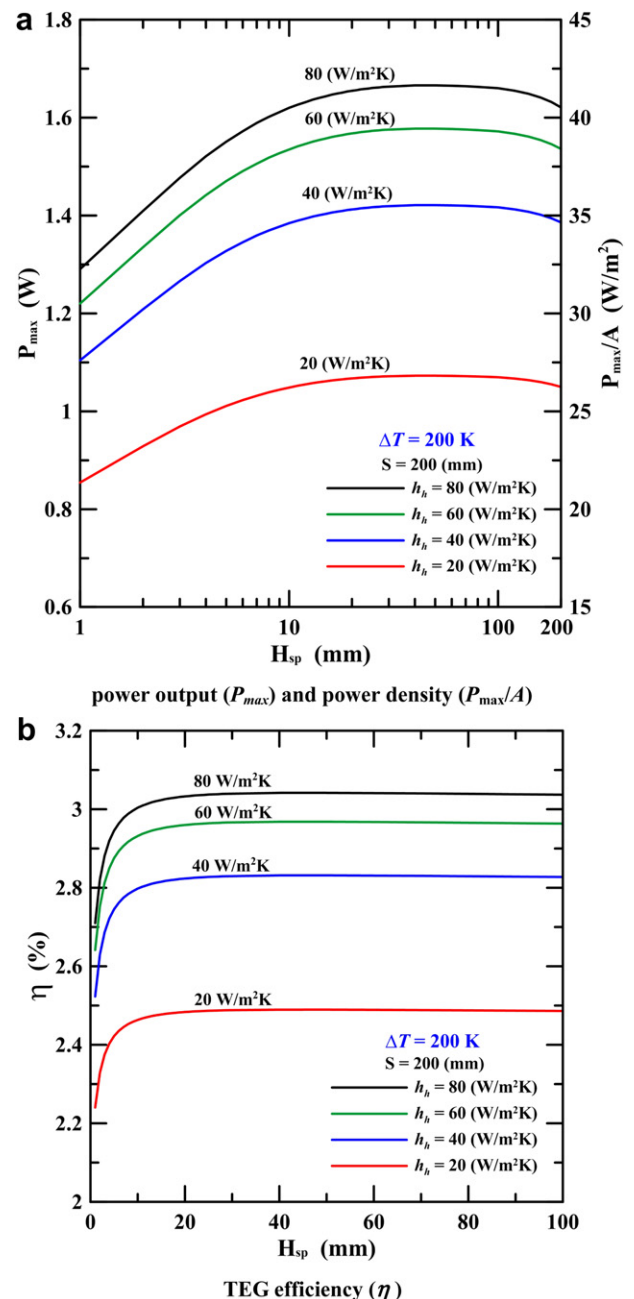


Fig. 9. The P_{max} , P_{max}/A and η vs. spreader thickness (H_{sp}) for different values of waste gas heat transfer coefficients with $S = 200 \text{ mm}$ and $\Delta T = 200 \text{ K}$.

between the waste gas and the cooling water ($\Delta T = 200, 400, 600$ and 800 K) with spreader thicknesses of $H_{sp} = 5$ mm and $h_h = 20$ W/m² K. It is evident that both the power output and TEG efficiency (η) are significantly increased as the temperature difference ΔT between the waste gas and the cooling water is increased. However, the optimum module spacing (S) for the maximum power density (P_{max}/A) is weakly dependent on ΔT . For example, for $H_{sp} = 5$ mm and $h_h = 20$ W/m² K, the optimal module spacing S is about 116 mm for $\Delta T = 200$ K, while the optimum $S = 112$ mm for $\Delta T = 800$ K.

Figs. 9 and 10 show the effect of the spreader thickness (H_{sp}) on P_{max} and η for different values of h_h and ΔT , respectively, with $S = 200$ mm. It can be seen that the power is first increased as the

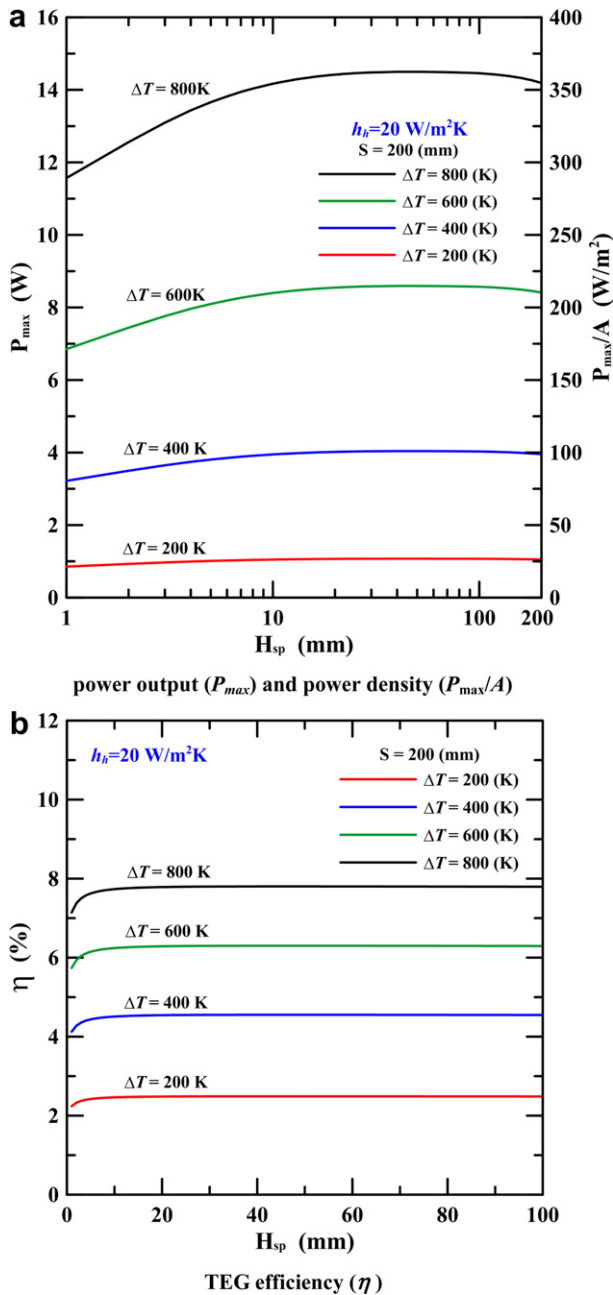


Fig. 10. The P_{max} , P_{max}/A and η vs. spreader thickness (H_{sp}) for different values of temperature differences between the waste gas and the cooling water with $S = 200$ mm and $h_h = 20$ W/m² K.

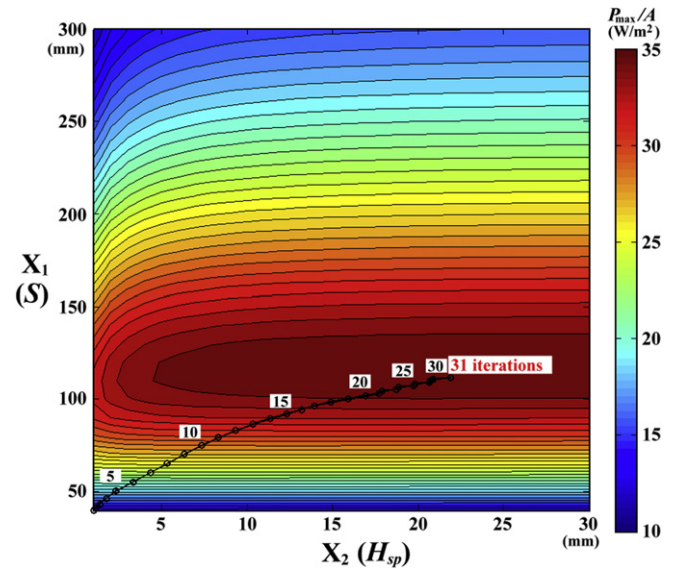


Fig. 11. Iteration process to search the optimum combination of S and H_{sp} for the maximization of objective function with $h_h = 20$ W/m² K and $\Delta T = 200$ K.

spreader thickness (H_{sp}) is increased. This is due to the fact that, as the spreader thickness is increased at the initial stage, there is an advantage of descending spreading resistance due to the path associated with the lateral heat diffusion from the hot waste gas to the TEG module. However, as the spreader thickness (H_{sp}) is increased over about 60 mm, there is greater thermal resistance penalty over the reduced spreading resistance, and thus, the power may be decreased. The TEG conversion efficiency (η) is increased as spreader thickness (H_{sp}) is increased. However, there is an asymptotic nature of the η – H_{sp} curves when H_{sp} is greater than around 10 mm.

Figs. 11–13 display three examples of the iteration process to search the optimum TEG module spacing (S) and its spreader thickness (H_{sp}) combination for the maximization of objective function (i.e. power density, P_{max}/A) for three operational

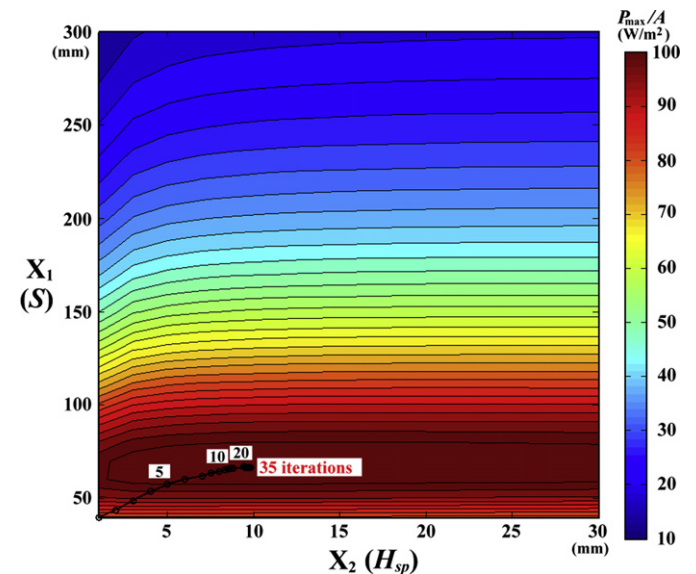


Fig. 12. Iteration process to search the optimum combination of S and H_{sp} for the maximization of objective function with $h_h = 60$ W/m² K and $\Delta T = 200$ K.

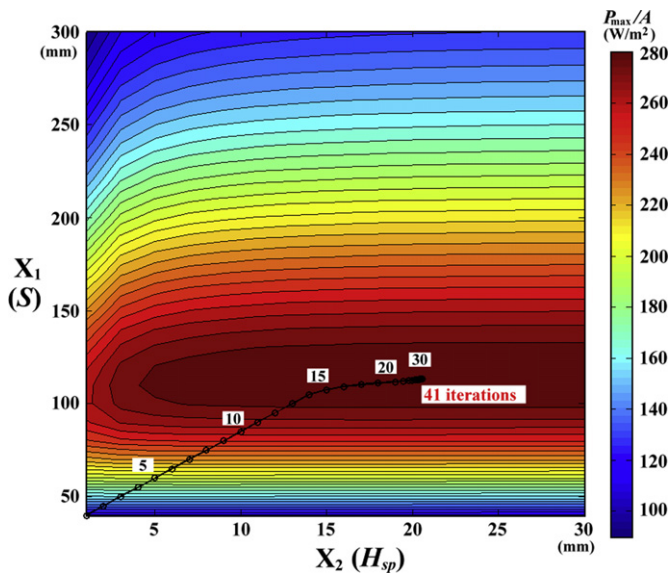


Fig. 13. Iteration process to search the optimum combination of S and H_{sp} for the maximization of objective function with $h_h = 20 \text{ W/m}^2 \text{ K}$ and $\Delta T = 600 \text{ K}$.

conditions (1) $h_h = 20 \text{ W/m}^2 \text{ K}$, $\Delta T = 200 \text{ K}$ (2) $h_h = 60 \text{ W/m}^2 \text{ K}$, $\Delta T = 200 \text{ K}$ (3) $h_h = 20 \text{ W/m}^2 \text{ K}$, $\Delta T = 600 \text{ K}$, respectively. The constant power density contours are plotted as a function of S and H_{sp} , where the dark brown area represents the maximum power density. It is noted that these constant power density contours were obtained by using 400 computer simulations for each plot. It is seen that, by using the simplified conjugated-gradient method (SCGM), the optimal S and H_{sp} combination can be obtained only for around 40 iterations (case 1: 31 iterations, case 2: 35 iterations, case 3: 41 iterations). Thus, the current optimization method provides a tremendous savings to computational time in the present study.

The searched optimum combination of S and H_{sp} for different operational conditions ($\Delta T = 200 - 800 \text{ K}$ and $h_h = 20 - 80 \text{ W/m}^2 \text{ K}$) is tabulated in Table 4. It can be seen that the optimum (S, H_{sp}) are strongly dependent on the waste gas heat transfer coefficient, h_h , and they are decreased as h_h is increased, while they are weakly dependent on the temperature difference between the waste gas and the cooling water, ΔT .

Table 4
The searched optimum combination of S and H_{sp} for different operational conditions.

ΔT (K)	h_h ($\text{W/m}^2 \text{ K}$)	S (mm)	H_{sp} (mm)
200	20	116.5	21.6
	40	82.3	13.3
	60	66.8	9.4
	80	58.1	7.1
400	20	114.6	20.9
	40	80.9	13.1
	60	66.0	9.3
	80	57.4	7.0
600	20	113.2	20.6
	40	79.9	12.9
	60	65.3	9.1
	80	56.8	6.9
800	20	112.4	20.3
	40	79.4	12.8
	60	64.8	9.0
	80	56.5	6.8

6. Conclusions

In this study, first, the parametric study for the thermal–electrical characteristics of a TEG module used in a waste heat recovery system was investigated numerically and experimentally. It was demonstrated that the proper size of a heat spreader can decrease the thermal resistance and that the maximum power P_{max} with a spreader can be significantly increased (up to 50%) as compared to TEG without spreader. The predicted numerical data for the power vs. current ($P-I$) curve are in good agreement (within 8%) with the experimental data. Secondly, the optimization of the TEG module spacing (S) and corresponding spreader thickness (H_{sp}) was performed by using a simplified conjugate-gradient method. The power density was the objective function to be maximized. The searched optimum combination of S and H_{sp} for different operational conditions ($\Delta T = 200 - 800 \text{ K}$ and $h_h = 20 - 80 \text{ W/m}^2 \text{ K}$) was obtained. The optimum TEG module spacing (S) and its spreader thickness (H_{sp}) were found to be strongly dependent on the waste gas heat transfer coefficient, h_h ; while they were weakly dependent on the temperature difference between the waste gas and the cooling water, ΔT . The results obtained in this study should provide useful information for the industrial TEG module design for waste heat recovery.

Acknowledgements

The financial support of this work provided by the China Steel Corporation of Taiwan is appreciated.

References

- [1] S.B. Riffat, X.L. Ma, Thermoelectrics: a review of present and potential applications, *Appl. Therm. Eng.* 23 (2003) 913–935.
- [2] A. Bejan, *Advanced Engineering Thermodynamics*, third ed., John Wiley & Sons, Hoboken, 2006.
- [3] S.W. Angrist, *Direct Energy Conversion*, fourth ed., Allyn and Bacon, Boston, 1992.
- [4] G. Min, D.M. Rowe, Optimization of thermoelectric module geometry for 'waste heat' electric power generation, *J. Power Sources* 38 (1992) 253–259.
- [5] D.M. Rowe, G. Min, Evaluation of thermoelectric modules for power generation, *J. Power Sources* 73 (1998) 193–198.
- [6] D.M. Rowe, A high performance solar powered thermoelectric generator, *Appl. Energy* 8 (1981) 269–273.
- [7] D.M. Rowe, Applications of nuclear-powered thermoelectric generators in space, *Appl. Energy* 40 (1991) 241–271.
- [8] J. Chen, Z. Yan, L. Wu, The influence of Thomson effect on the maximum power output and maximum efficiency of a thermoelectric generator, *J. Appl. Phys.* 79 (1996) 8823–8828.
- [9] X.C. Xuan, K.C. Ng, C. Yap, H.T. Chua, A general model for studying effects of interface layers on thermoelectric devices performance, *Int. J. Heat Mass Transfer* 45 (2002) 5159–5170.
- [10] A.K. Pramanick, P.K. Das, Constructural design of a thermoelectric device, *Int. J. Heat Mass Transfer* 49 (2006) 1420–1429.
- [11] K. Ono, R.O. Suzuki, Thermoelectric power generation: converting low-grade heat into electricity, *JOM* 50 (1998) 49–51.
- [12] D.M. Rowe, Thermoelectrics, an environmentally-friendly source of electrical power, *Renew. Energy* 16 (1999) 1251–1256.
- [13] N.M. Khattab, E.T. El Shenawy, Optimal operation of thermoelectric cooler driven by solar thermoelectric generator, *Energy Convers. Manag.* 47 (2006) 407–426.
- [14] D.T. Crane, G.S. Jackson, Optimization of cross flow heat exchangers for thermoelectric waste heat recovery, *Energy Convers. Manag.* 45 (2004) 1565–1582.
- [15] D. Dai, Y. Zhou, J. Liu, Liquid metal based thermoelectric generation system for waste heat recovery, *Renew. Energy* 36 (2011) 3530–3536.
- [16] D. Champier, J.P. Bedecarrats, M. Rivaletto, F. Strub, Thermoelectric power generation from biomass cook stoves, *Energy* 35 (2010) 935–942.
- [17] Y.Y. Hsiao, W.C. Chang, S.L. Chen, A mathematic model of thermoelectric module with applications on waste heat recovery from automobile engine, *Energy* 35 (2010) 1447–1454.
- [18] E.F. Thacher, B.T. Helenbrook, K.A. Karri, C.J. Richter, Testing of an automobile exhaust thermoelectric generator in a light truck, *Proc. Inst. Mech. Eng. Part. D J. Automob. Eng.* 221 (2007) 95–107.
- [19] X. Niu, J. Yu, S. Wang, Experimental study on low-temperature waste heat thermoelectric generator, *J. Power Sources* 188 (2009) 621–626.
- [20] M.A. Karri, E.F. Thacher, B.T. Helenbrook, Exhaust energy conversion by thermoelectric generator: two case studies, *Energy Convers. Manag.* 52 (2011) 1596–1611.

- [21] A.J. Minnich, M.S. Dresselhaus, Z.F. Ren, G. Chen, Bulk nanostructured thermoelectric materials: current research and future prospects, *Energy Environ. Sci.* 2 (2009) 466–479.
- [22] M. Chen, L.A. Rosendahl, T. Condra, A three-dimensional numerical model of thermoelectric generators in fluid power systems, *Int. J. Heat Mass Transfer* 54 (2011) 345–355.
- [23] C.H. Cheng, S.Y. Huang, T.C. Cheng, A three-dimensional theoretical model for predicting transient thermal behavior of thermoelectric coolers, *Int. J. Heat Mass Transfer* 53 (2010) 2001–2011.
- [24] O. Sidek, M.Z. Ishak, M.A. Miskam, Study on temperature uniformity of thermal spreader integration with microcombustor for thermoelectric power generator, in: *Proceedings of the International Conference on Electrical, Control and Computer Engineering*, 2011, pp. 526–530.
- [25] J.Y. Jang, Y.C. Tsai, Y.C. Huang, Optimal design of the heat spreader applied thermoelectric module for waste heat recovery, *Adv. Sci. Lett.* 14 (2012) 253–257.
- [26] J.Y. Jang, C.H. Cheng, Y.X. Huang, Optimal design of baffles locations with interdigitated flow channels of a centimeter-scale proton exchange membrane fuel cell, *Int. J. Heat Mass Transfer* 53 (2010) 732–743.
- [27] F.P. Incropera, D.P. DeWitt, *Fundamentals of Heat and Mass Transfer*, John Wiley & Sons, 2002.
- [28] R.J. Moffat, Describing the uncertainties in experimental results, *Exp. Therm. Fluid Sci.* 1 (1988) 3–17.